Banner appropriate to article type will appear here in typeset article

Drag reduction on a transonic wing

Maurizio Quadrio[1], Alessandro Chiarini[1], Jacopo Banchetti[1], Davide Gatti[2], Antonio Memmolo[3], Sergio Pirozzoli[4]

[1]Dipartimento di Scienze e Tecnologie Aerospaziali, Politecnico di Milano, via La Masa 34, 20156 Milano, Italy

[2]Institute for Fluid Mechanics, Karlsruhe Institute of Technology, Kaiserstr. 10, 76131 Karlsruhe, Germany

[3]High Performance Computing Department, CINECA-Interuniv. Cons., 40033 Bologna, Italy

[4]Dipartimento di Ingegneria Meccanica e Aerospaziale, La Sapienza Univ. Roma, Via Eudossiana, Roma, Italy

Flow control for turbulent skin-friction drag reduction is applied to a transonic wing to improve its aerodynamic performance. The study is based on direct numerical simulations (with up to 1.8 billions cells) of the compressible turbulent flow around a wing slab, at Reynolds and Mach numbers of $Re_\infty = 3 \times 10^5$ and $M_\infty = 0.7$. Control is applied only on a portion of the suction side of the wing. Besides locally reducing friction, the control modifies the shock wave and significantly improves the aerodynamic efficiency of the wing by increasing lift and decreasing drag. The wing, therefore, achieves the required lift with a lower angle of attack and with a lower drag. Estimates of the benefits for the whole aircraft indicate that substantial savings are possible; the energy cost of the possibly active control is negligible thanks to the small application area. We suggest that skin-friction drag reduction should be considered not only as a goal, but also as a tool to improve the global aerodynamics of complex flows.

Key words:

1. Introduction

The importance of flow control for the reduction of turbulent skin-friction drag is steadily growing over the years, because of a combination of efficiency and environmental reasons. Unfortunately, to date only few strategies have been deployed in real-world applications, owing to an often critical cost/benefit ratio. One of the key drawbacks is that benefits of both passive (e.g. riblets) and active techniques are proportional to the fraction of the surface covered by the drag-reducing device, with a partial coverage leading only to partial benefits.

Most of the research and development of skin-friction drag reduction techniques has taken place in parallel duct flows, where the drag force is entirely due to

Abstract must not spill onto p.2

friction. However, the practical appeal of drag reduction in duct flows is limited, as their energetic efficiency can be trivially improved by enlarging the cross-section of the duct. The pumping energy required to sustain a certain flow rate is proportional to the hydraulic radius r_h^{-5}: a small increase of r_h would reduce energy consumption easily and at a relatively small capital cost.

In more complex flows, where the aerodynamic drag contains additional contributions besides the viscous friction, such as pressure drag, parasitic drag, lift-induced drag and wave drag, what ultimately matters is reducing the overall drag. Recent are the first attempts of the research community to consider how skin-friction reduction affects the other drag contributions. Banchetti *et al.* (2020) applied spanwise forcing via streamwise-travelling waves in a channel flow where one wall has a bump that creates pressure drag. They found that a distributed reduction of friction affects favourably the pressure field and that the combined friction and pressure drag reduction increases by one half the net energetic benefits. Similarly, Nguyen *et al.* (2021) determined the beneficial effects of a temporally spanwise-oscillating pressure gradient in a channel flow with transverse bars at the wall and found that pressure drag is reduced as nearly as friction drag, although the overall net energy budget remains slightly negative.

Perhaps the most obvious application where drag reduction entails significant benefits is the airplane, where the aerodynamic efficiency is key. Atzori *et al.* (2020) studied with high-fidelity Large Eddy Simulations (LES) the effect of uniform blowing or suction on the incompressible flow past a wing slab built with the NACA4412 airfoil at a Reynolds number (based on free-stream velocity and chord length) of $Re = 200,000$. They found that the wing efficiency improves up to 11% when uniform suction is applied on the suction side, enforcing friction drag increase but pressure drag reduction. Kornilov (2021) carried out an experimental study of blowing/suction on two-dimensional low-speed airfoils and provided an ideal estimate of the power spent for actuation. Albers & Schröder (2021) studied with implicit LES the same airfoil considered by Atzori *et al.* (2020), but controlled the flow via spanwise-travelling waves of wall-normal deformation. They generalised their previous results based on a different wing section (Albers *et al.* 2019) and demonstrated that the control is capable of altering both friction and pressure drag, leading to an increase of the overall aerodynamic performances of the wing.

All these works have considered the flow in the incompressible or subsonic regimes. However, there are reasons to suspect (see e.g. Mele *et al.* 2016) that one further advantage of reducing skin friction resides in the ability to interact with the position and strength of the shock wave generated over the wing in the transonic regime. Since civil aircraft cruise and military aircraft maneuver in the transonic regime, this would be important in assessing the effectiveness of flow control for aeronautical applications. In this work we present the first direct numerical simulation (DNS) of the compressible turbulent flow over a wing slab in the transonic regime, where flow control for skin-friction reduction is applied. We explore to what extent a localised control for skin-friction reduction interacts with the shock and alters the aerodynamic performances of the wing. The results are also extrapolated to the entire aircraft. The active control technique chosen for the study is the streamwise-traveling waves of spanwise forcing (Quadrio *et al.* 2009), which offers the advantages of producing large (hence easily measurable) effects and large net savings as well. However, the general conclusions are valid for any skin-friction reduction technology.
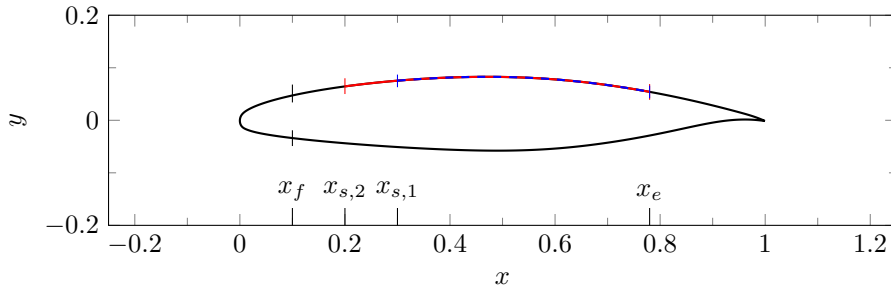
Figure 1: Shape of the V2C transonic airfoil. Volume forcing is applied at x_f (on both sides) to initiate transition. x_s and x_e denote start and end of the suction-side actuated region for cases C1 (blue dashed line) and C2 (red continuous line).

2. Methods

We study by DNS the transonic flow around a wing slab XXX SERGIO: SCEGLI LE PAROLE GIUSTE! made by the V2C airfoil (see figure 1), a supercritical airfoil designed by Dassault Aviation in the context of the European research program TFAST XXX. The Reynolds and Mach numbers of the flow are set to $Re_\infty = U_\infty c/\nu_\infty = 3 \times 10^5$ and $M_\infty = U_\infty/a_\infty = 0.7$, where c is the airfoil chord and U_∞, ν_∞ and a_∞ are the free-stream velocity, kinematic viscosity and sound speed. c and U_∞ are the reference length and velocity, unless otherwise noted. The x, y and z axes denote the chordwise, vertical and spanwise directions. The angle of attack is $\alpha = 4°$, which corresponds to the maximum aerodynamic efficiency of the profile at this Re_∞ and M_∞. The DNS code (see Memmolo *et al.* 2018, for a detailed description) solves the compressible Navier–Stokes equations for a calorically perfect gas. It is based on a second-order finite volumes method, which switches to third-order WENO scheme according to a modified Ducros sensor (Ducros *et al.* 1999). Time advancement uses a low-storage, third-order Runge–Kutta scheme. At the farfield, characteristics-based non-reflective boundary conditions are used (Poinsot & Lelef 1992), while periodicity is enforced in the spanwise direction. Discretisation is based on a C-type mesh, with radius of $25c$; the outflow is placed at $25c$ from the trailing edge. In the spanwise z direction the domain extends for $0.1c$ to ensure decorrelation of all the flow structures on the airfoil and in the wake (Zhang & Samtaney 2016; Hosseini *et al.* 2016). The incoming flow is laminar. As done by Schlatter & Örlü (2012), transition to turbulence is enforced on both sides of the airfoil via a volume force located at $x = x_f = 0.1c$.

Streamwise-travelling waves of spanwise velocity are applied on a portion of the suction side of the wing. The spanwise velocity component w_w applied at the wall is:

$$w_w(x,t) = f(x)A \sin\left(\kappa_x x - \omega t\right)$$

where A is the maximum forcing amplitude and κ_x and ω are the spatial and temporal frequencies of the wave. As in Yudhistira & Skote (2011), a smoothing function $f(x)$ is used to raise the spanwise velocity at the initial position x_s and then return it to zero at x_e. The tuning of the forcing, as well as the choice of x_s and x_e, would by themselves deserve a detailed investigation. In this work, only two configurations are considered, hereinafter referred to as C1 and C2.

They have been set up after a preliminary parametric study and correspond to different forcing strengths, so that the stronger C2 produces flow separation after the shock wave, whereas C1 almost does not. In both cases the actuated region starts after the tripping and ends after the shock wave. C1 has $x_s = 0.3$, $x_e = 0.78$, $A = 0.5$, $\omega = 11.3$ and $\kappa_x = 161$. In C2 the actuated region is longer starting $x_s = 0.2$, and the forcing amplitude is larger, i.e. $A = 0.684$. For C2, this corresponds to $A^+ \approx 6.6$, $\omega^+ \approx 0.06$ and $\kappa_x^+ \approx 0.013$ after expressing quantities in viscous units computed with the average value of the friction velocity along the actuated region: this is not far from the incompressible channel flow maximum net saving, yielding about 33% drag reduction and 20% net power savings at a friction Reynolds number of $Re_\tau = 200$.

Six DNS are carried out. Four of them use the baseline grid with 536 million points and include no-control, C1 and C2 (the latter repeated at a different angle of attack, see later §3.3). This mesh is comparable to the mesh used by Zauner *et al.* (2019) on the same profile and at a slightly larger $Re_\infty = 5 \times 10^5$. No-control and C2 are also run on a finer grid with 1.8 billions points to validate the results. The baseline grid has $4096 \times 512 \times 256$ points, with an uniform distribution in the spanwise direction and a hyperbolic-tangent distribution in the other directions to increase resolution close to the airfoil and in the wake. The finer grid made by $6144 \times 768 \times 384$ points is obtained by increasing their number by 50% in each direction. An *a posteriori* check has confirmed that at the wall the requirement for a fully-resolved DNS (Hosseini *et al.* 2016) of $\Delta x^+ < 10, \Delta y^+ < 0.5, \Delta z^+ < 5$ are satisfied. The simulations are advanced with a constant time step Δt chosen to maintain the maximum Courant–Friedrichs–Lewy number below unity; it is $\Delta t = 1.5 \times 10^{-4}$ for the baseline grid and $\Delta t = 1 \times 10^{-4}$ for the fine grid. Flow statistics are accumulated for $40c/U_\infty$ after reaching statistical equilibrium.

3. Results

3.1. *Instantaneous and mean fields*

An overview of the mean and instantaneous fields in the no-control case is provided by figure 2, where instantaneous vortical structures are visualised via isosurfaces of the imaginary part of the complex conjugate eigenvalue pair of the velocity gradient tensor $\Im(\lambda_{ci})$ (Zhou *et al.* 1999), together with the location of the shock. The mean Mach number is plotted in the background. The three sonic lines at $M = 1$ are shown for the no-control (red), C1 (blue) and C2 (green) cases. The flow becomes supersonic at the nose and remains laminar up to the tripping. The supersonic region extends up to $x \approx 0.5c$, where the flow undergoes abrupt recompression due to the shock wave. The control moves the shock downstream, enlarging the supersonic region: its streamwise and vertical dimensions increase from $D_x = 0.47c$ and $D_y = 0.35c$ (no-control) to $D_x = 0.48c, D_y = 0.36c$ (C1) and $D_x = 0.52c, D_y = 0.42c$ (C2). The shock wave intensity increases too and the pressure jump across the shock, measured for example at $y = 0.2$, increases from $\Delta p = 0.121$ (no-control) to $\Delta p = 0.136$ (C1) and $\Delta p = 0.167$ (C2). Consistently, the maximum Mach number increases from $M = 1.087$ (no-contro) to $M = 1.093$ (C1) and $M = 1.116$ (C2), while its position remain almost unchanged at $(x, y) \approx (0.39c, 0.094c)$. These flow modifications are consistent with a decreased friction in the actuated region, leading to an increase of the supersonic flow speed.
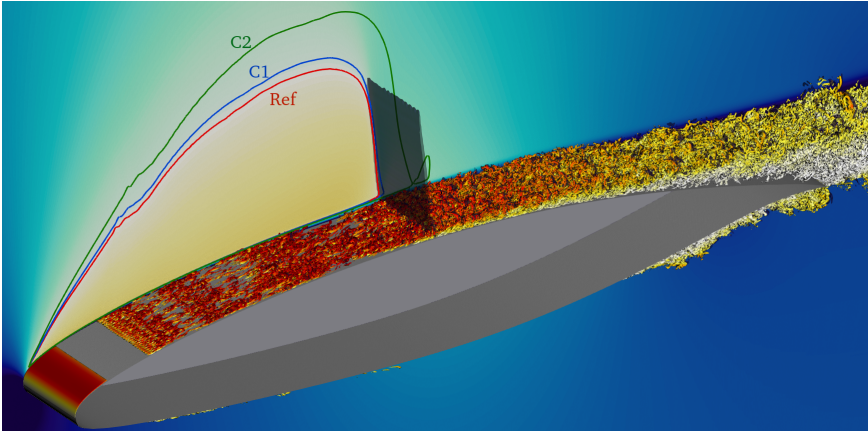
Figure 2: Turbulent structures in an instantaneous snapshot of the reference case, visualised via isosurfaces of the swirling strength $\Im(\lambda_{ci}) = 100$, and coloured with the turbulent kinetic energy k (white-to-red colormap for $0 \leqslant k \leqslant 1$). The background colour map is for the mean Mach number (symmetric blue-to-red colormap for $0.5 \leqslant M \leqslant 1.5$). Sonic lines at $M = 1$ are drawn for reference (red), C1 (blue) and C2 (green). The shock wave is identified by the grey isosurface plotted for $\partial\rho/\partial x = 10$.
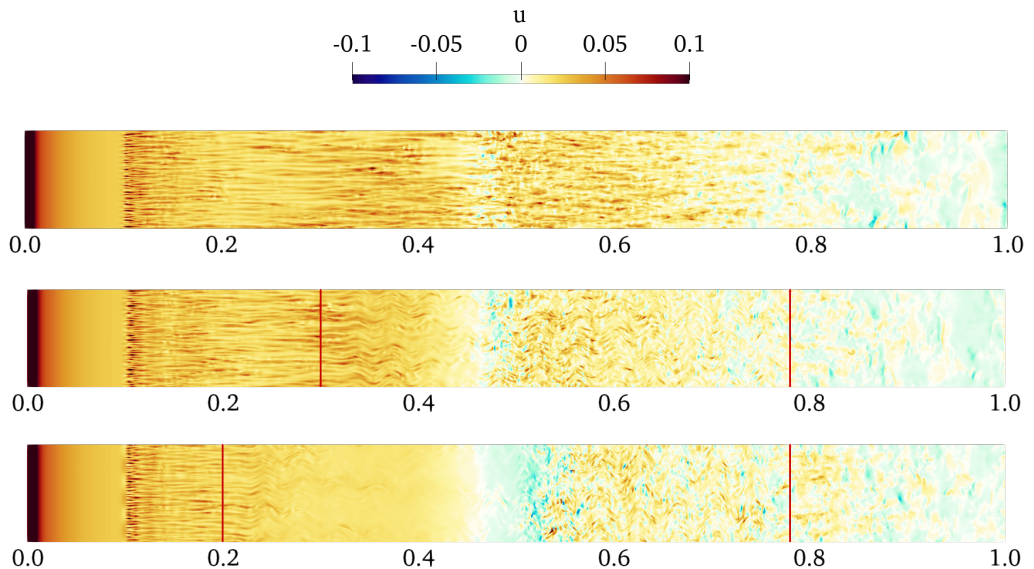

Figure 3: Instantaneous chordwise velocity component at the first grid point off the wing surface over the suction side, for no-control (top), C1 (middle) and C2 (bottom). The red lines mark the boundaries of the actuated region.

The development of the near-wall flow along the suction side of the airfoil is visualised in figure 3 for the three cases, where the instantaneous chordwise velocity component is plotted at the first grid point off the wall, i.e. $y \approx 3 \cdot 10^{-5} c$, thus providing a qualitative proxy for the skin friction at the wall. The boundary layer is confirmed to be laminar up to the tripping, which generates a pattern of alternating low- and high-speed streaks. Then, in the reference case the
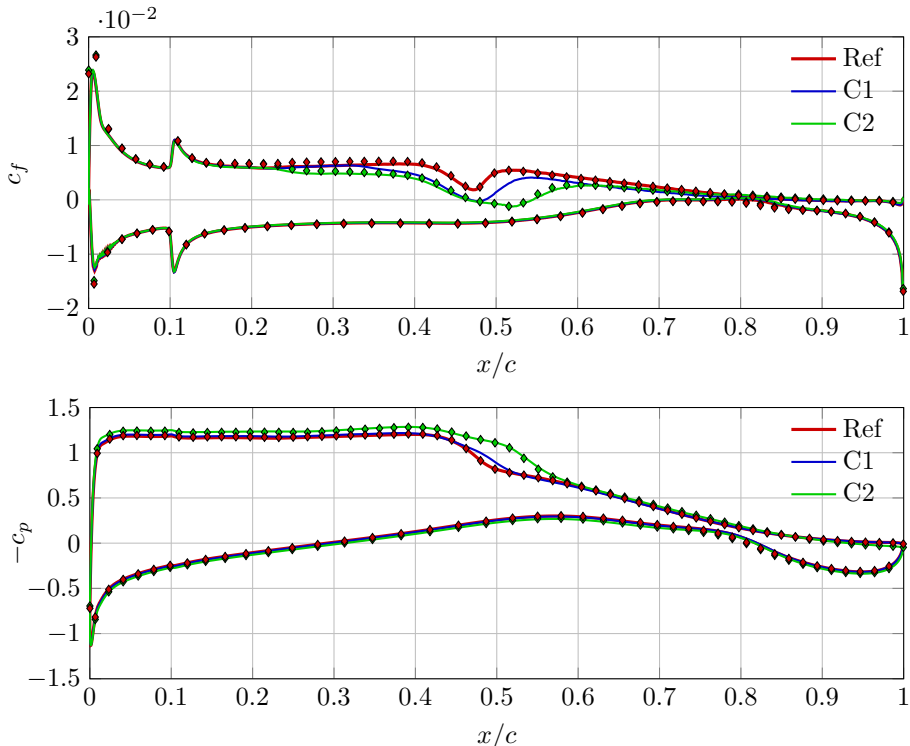
Figure 4: Friction coefficient c_f (top) and pressure coefficient c_p (bottom).
Reference and C2 results obtained on the finer grid are shown with symbols.
(Note that on the pressure side green and red symbols almost overlap.

fluctuations undergo a transient decay and a further growth up to $x \approx 0.46c$, where the interaction with the shock wave causes a sharp decrease. Immediately after x_s, the control produces visible spanwise oscillations in the developing streaks and reduces turbulent activity, so that the streaks almost disappear at $x_s + 0.1c$, and the flow almost relaminarises before the shock wave. Immediately after the shock, the no-control case shows few spots with backflow ($u < 0$), while in the controlled cases the local backflow after the shock wave is more intense, especially for C2, indicating a separation of the boundary layer.

3.2. *Wall friction and pressure*

Figure 4 plots the mean friction and pressure coefficients $c_f = 2\tau_w/(\rho_\infty U_\infty^2)$ and $c_p = 2(p - p_\infty)/(\rho_\infty U_\infty^2)$. $\tau_w = \mu \hat{\boldsymbol{t}} \cdot \partial \boldsymbol{u}/\partial n$ is the wall shear stress, with $\hat{\boldsymbol{t}}$ being the tangential unit vector and $\partial/\partial n$ the derivative in the wall-normal direction. μ, ρ and p are the dynamic viscosity, density and pressure. Solid lines are results from the baseline grid, while symbols are from the fine grid used for validation.

Results from the two grids are overlapping, especially for c_p. Only the peak of c_f in the relatively unimportant region of the airfoil nose turns out to be slightly under-resolved by the baseline grid. Changes between no-control and actuated cases are, however, very well predicted by the baseline grid.

Since on the pressure side there is no actuation and the curves are virtually unchanged, only the suction side is considered. After the leading-edge peak, c_f

	Ref	C1	Δ_1	C2	Δ_2	C2 ($\alpha = 3.45°$)	Δ_2
$C_{d,f}$	0.0082	0.0076	-7.3%	0.0071	-13.4%	0.0074	-9.7%
$C_{d,p}$	0.0165	0.0161	-2.4%	0.0174	+5.5%	0.0136	-17.6
C_d	0.0247	0.0236	-4.5%	0.0245	-0.8%	0.0210	-15.0%
C_l	0.740	0.751	+1.5%	0.825	+11.3%	0.730	-1.3%
C_l/C_d	29.7	31.7	+6.8%	33.7	+13.5%	34.8	+17.2%

Table 1: Lift and drag coefficients C_l and C_d, and decomposition of drag coefficient into friction and pressure contributions $C_{d,f}$ and $C_{d,p}$, for reference, C1 and C2. Δ stands for relative change, and the last two columns refer to C2, but computed at an angle of attack of $\alpha = 3.45°$.

decreases rapidly in the laminar region up to x_f, where the effect of the numerical tripping is distinctly visible. Further downstream, c_f suddenly drops because of the shock-wave/boundary-layer interaction at $x \approx 0.45c$ and then, after increasing again, it slowly decreases to eventually become negative just before the trailing edge, where the flow separates. In the no-control case, despite the negative u fluctuations observed in the instantaneous field in figure 3, c_f remains positive after the shock wave. In the controlled cases, after x_s the forcing effectively reduces friction in the actuated part of the surface. As expected (Quadrio & Ricco 2004; Skote 2012), a spatial transient exists where drag reduction develops. Once this is accounted for, the local skin-friction reduction is in line with the expectation based on incompressible channel flow information. In both controlled cases c_f becomes negative after the shock wave: the mean recirculation extends for $0.46c \leqslant x \leqslant 0.49c$ for C1, and for $0.46c \leqslant x \leqslant 0.54c$ for C2 with stronger forcing, in agreement with the instantaneous visualisation of figure 3.

The pressure coefficient, after the expansion at the leading edge, features a flat plateau which extends up to the shock compression, as per the design of the transonic profile. Then, in the rear part c_p progressively increases and becomes null at the trailing edge. In the controlled cases two distinct effects are observed, which contribute both to an increase of the suction: the compression associated with the shock wave is moved downstream and the expansion at the leading edge is stronger. The recirculating region in the controlled cases decreases the adverse pressure gradient in the area near the shock, producing a milder slope of c_p in correspondence of the pressure recovery before the shock-induced compression. Thus the shock wave moves downstream and enlarges the supersonic bubble, resulting in an increase of the velocity within the bubble and, therefore, in a stronger expansion in the fore part of the airfoil. Both effects are more evident in C2, designed to produce an evident recirculation after the shock wave. Overall, the control changes the c_p distribution in a way that is consistent with a slight increase of the free-stream Mach number, but only on the suction side.

3.3. *Aerodynamic forces and extrapolation*

The control-induced changes to the distributions of friction and pressure positively affect both lift and drag. Table 1 compares the lift and drag coefficients C_l and C_d for the no-control and controlled cases. Friction and pressure contributions to the total drag are computed separately and reported as $C_{d,f}$ and $C_{d,p}$. The control action reduces the friction share of the total drag by 7.3% and 13.4% for

C1 and C2. These are substantial reductions, considering that control is applied only on about one quarter of the total surface. As expected, the friction drag reduction is larger for C2, owing to its longer actuated region and stronger intensity. The control-induced variation of the pressure drag, instead, has a different sign in the two cases: $C_{d,p}$ decreases by 2.4% for C1 and increases by 5.5% for C2. The combined changes result into a reduction of the total drag for both cases, quantified by 4.5% for C1 and by a marginal 0.8% for C2. However, a crucial effect is the increase of the lift coefficient. In agreement with the changes in the pressure distribution shown in figure 4, the increase of C_l is minor for C1 (+1.5% only), but quite large for C2 (+11.3%). The wing efficiency, therefore, is significantly enhanced in both cases, by 6.8% for C1 and 13.5% for C2.

Increasing the wing efficiency implies that the lift required to balance the aircraft weight can be obtained at a lower angle of attack and, therefore, at the cost of a lower drag. One can preliminarily estimate the additional gain in drag reduction by assuming that the control-induced relative changes of the aerodynamic forces remain constant for small changes of α. The characteristics curves $C_l - \alpha$ and $C_d - \alpha$ have been evaluated, in absence of control, with additional Reynolds Averaged Navier–Stokes (RANS) simulations, carried out with a modified version of the code described in §2 and a Spalart–Allmaras turbulence model. For C1, the $C_l - \alpha$ curve shows that the angle of attack can be reduced to $\alpha = 3.92°$, yielding an extra drag reduction of about 1.2%, for a total 5.7%. For C2, the reduction of angle of attack is larger at $\alpha = 3.45°$, yielding an extra drag reduction of 9.0%, and a total of 9.9%. Only for this case, an additional DNS at the target $\alpha = 3.45°$ has been performed, and its results are shown in the last two columns of table 1. The obtained lift coefficient is $C_l = 0.730$, i.e. slightly lower than the required value by 1.3%, but the drag coefficient decreases to $C_d = 0.0210$, yielding a drag reduction of about 15%.

It is instructive to try and scale these figures to the aircraft level. As an example, we consider the wing-body configuration DLR-F6 defined in the Second AIAA CFD Prediction Workshop (Laflin *et al.* 2005), with flight conditions of $M_\infty = 0.75$ and $Re_\infty = 3 \cdot 10^6$. The reference lift coefficient is $C_L = 0.5$, obtained at an angle of attack of $\alpha = 0.52°$ at the cost of $C_D = 0.0295$. We look for the achievable drag reduction when the control C2 is applied. In doing this, the following simplifying assumptions are made: (i) the wing is responsible for the entire lift and for 1/3 of the drag; (ii) changes ΔC_l and ΔC_d induced by control are constant along the wing span, and do not change with α, M_∞ and Re_∞, so that the values reported in Table 1 apply. Using experimental data at `https://aiaa-dpw.larc.nasa.gov/Workshop2/DPW_forces_WB_375`, we estimate that the application of the C2 control allows a reduced angle of attack of $\alpha = 0.0125°$, yielding $C_D = 0.0272$ and, therefore, a drag reduction of approximately 8.5%, which should be further incremented by the additional 0.8% that directly follows from skin-friction reduction, yielding a reduction by 9.3% of the aircraft drag. The actuation power required by C2 is very small. Based on channel flow data, the forcing power for the C2 control is about 14% of the power spent against friction drag over the actuated surface. However, the control is rather localised, with the actuated area being approximately one-fourth of the wing surface and one twelfth of the entire aircraft surface. The actuation power is therefore around 1% of the friction power; since friction drag on the aircraft is about one half of the total drag (Abbas *et al.* 2013), one is left with a power cost of only 0.5% of the total power.

4. Concluding discussion

We have reported the first DNS of the controlled compressible turbulent transonic flow over a wing slab at $M_\infty = 0.7$ and $Re_\infty = 3 \times 10^5$. The aerodynamic performance of the wing is improved by using active spanwise wall forcing to reduce the skin friction locally on a portion of the suction side of the wing.

The locally reduced friction modifies position and strength of the shock wave, causing a stronger expansion in the fore part and a delayed, more intense shock. Overall, this is equivalent to an increase of the Mach number, but on the suction side only, and yields a large improvement of the lift/drag ratio. In the most effective considered case, the aerodynamic efficiency increases by 13.5% (with drag decreased by 0.8% only). The higher aerodynamic efficiency implies that the required lift is achieved at a lower angle of attack, yielding a significant reduction of the total drag which has been measured by DNS to be about 15%. We have then estimated that this may lead to a total drag reduction of about 9% for the entire aircraft in cruise flight, and that the energy cost for the active control would be nearly negligible. The fact that control can be applied locally to achieve global significant benefits is of enormous importance in terms of both practical feasibility and benefit/cost ratio.

We close the paper with a brief discussing its limitations. First of all, the reported drag reduction of 9% should in no way be taken as the maximum achievable gain. Indeed, the available forcing information for incompressible channel flow (or flat plate boundary layer) cannot be straightforwardly translated to an airplane in cruise flight; moreover, the plane-channel situation of maximum power saving may well be far from the optimum when the whole drag is concerned. Locating where and when and how much the control should be activated is an entirely new problem, whose solution might grant much better performance. Moreover, while the M_∞ value considered here is representative of an airplane in transonic flight, Re_∞ is not: a serious design attempt should consider higher Re. Luckily, we know already (Gatti & Quadrio 2016) that spanwise forcing and, more in general, skin-friction drag reduction techniques remain effective at higher Re. However, a different target flow at much higher Re_∞ will certainly require different details of the optimisation. Finally, one should always be aware of the challenge of designing actuators capable to meet the required specification with an acceptable energy efficiency. The general idea discussed here, though, is valid for any control, including passive strategies, e.g. riblets.

All in all, we believe that considering skin-friction drag reduction as a tool and not only as a goal in flows where friction drag is not the key target for optimisation will open new avenues to a widespread use of flow control.

Declaration of Interests

The authors report no conflict of interest.

REFERENCES

ABBAS, A., DE VICENTE, J. & VALERO, E. 2013 Aerodynamic technologies to improve aircraft performance. *Aerospace Science and Technology* **28** (1), 100–132.

ALBERS, M., MEYSONNAT, P. S. & SCHRÖDER, W. 2019 Actively Reduced Airfoil Drag by Transversal Surface Waves. *Flow Turbulence Combust* **102** (4), 865–886.

ALBERS, M. & SCHRÖDER, W. 2021 Lower drag and higher lift for turbulent airfoil flow by moving surfaces. *International Journal of Heat and Fluid Flow* **88**, 108770.

ATZORI, M., VINUESA, R., FAHLAND, G., STROH, A., GATTI, D., FROHNAPFEL, B. & SCHLATTER, P. 2020 Aerodynamic Effects of Uniform Blowing and Suction on a NACA4412 Airfoil. *Flow Turbulence Combust* **105** (3), 735–759.

BANCHETTI, J., LUCHINI, P. & QUADRIO, M. 2020 Turbulent drag reduction over curved walls. *J. Fluid Mech.* **896**.

DUCROS, F, FERRAND, V, NICOUD, F, WEBER, C, DARRACQ, D, GACHERIEU, C & POINSOT, T 1999 Large-Eddy Simulation of the Shock/Turbulence Interaction. *Journal of Computational Physics* **152** (2), 517–549.

GATTI, D. & QUADRIO, M. 2016 Reynolds-number dependence of turbulent skin-friction drag reduction induced by spanwise forcing. *J. Fluid Mech.* **802**, 553–58.

HOSSEINI, S. M., VINUESA, R., SCHLATTER, P., HANIFI, A. & HENNINGSON, D. S. 2016 Direct numerical simulation of the flow around a wing section at moderate Reynolds number. *International Journal of Heat and Fluid Flow* **61**, 117–128.

KORNILOV, V. 2021 Combined Blowing/Suction Flow Control on Low-Speed Airfoils. *Flow Turbulence Combust* **106** (1), 81–108.

LAFLIN, K.R., KLAUSMEYER, S.M., ZICKUHR, T., VASSBERG, J.C., WAHLS, R.A., MORRISON, J.H., BRODERSEN, O.P., RAKOWITZ, M.E., TINOCO, E.N. & GODARD, J.-L. 2005 Data Summary from Second AIAA Computational Fluid Dynamics Drag Prediction Workshop. *J. Aircraft* **42** (5), 1165–1178.

MELE, B., TOGNACCINI, R. & CATALANO, P. 2016 Performance assessment of a transonic wing-body configuration with riblets installed. *J. Aircr.* **53** (1), 129–140.

MEMMOLO, A., BERNARDINI, M. & PIROZZOLI, S. 2018 Scrutiny of buffet mechanisms in transonic flow. *Int. J. Numer. Methods Heat Fluid Flow* **28** (5), 1031–1046.

NGUYEN, V.-T., RICCO, P. & PIRONTI, G. 2021 Separation drag reduction through a spanwise oscillating pressure gradient. *J. Fluid Mech.* **912**.

POINSOT, T. J & LELEF, S. K 1992 Boundary conditions for direct simulations of compressible viscous flows. *J. Comp. Phys.* **101** (1), 104–129.

QUADRIO, M. & RICCO, P. 2004 Critical assessment of turbulent drag reduction through spanwise wall oscillation. *J. Fluid Mech.* **521**, 251–271.

QUADRIO, M., RICCO, P. & VIOTTI, C. 2009 Streamwise-traveling waves of spanwise wall velocity for turbulent drag reduction. *J. Fluid Mech.* **627**, 161–178.

SCHLATTER, P. & ÖRLÜ, R. 2012 Turbulent boundary layers at moderate Reynolds numbers: Inflow length and tripping effects. *J. Fluid Mech.* **710**, 5–34.

SKOTE, M. 2012 Temporal and spatial transients in turbulent boundary layer flow over an oscillating wall. *Int. J. Heat Fluid Flow* **38**, 1–12.

YUDHISTIRA, I. & SKOTE, M. 2011 Direct numerical simulation of a turbulent boundary layer over an oscillating wall. *J Turbul.* **12** (9), 1–17.

ZAUNER, M., DE TULLIO, N. & SANDHAM, N. D. 2019 Direct Numerical Simulations of Transonic Flow Around an Airfoil at Moderate Reynolds Numbers. *AIAA J.* **57** (2), 597–607.

ZHANG, W. & SAMTANEY, R. 2016 Assessment of spanwise domain size effect on the transitional flow past an airfoil. *Computers and Fluids* **124**, 39–53.

ZHOU, J., ADRIAN, R. J., BALACHANDAR, S. & M., KENDALL T. 1999 Mechanisms for generating coherent packets of hairpin vortices in channel flow. *J. Fluid Mech.* **387**, 353–396.

Rapids articles must not exceed this page length